Ru nanoparticles supported on partially reduced TiO2 as highly efficient catalyst for hydrogen evolution

Ru nanoparticles supported on partially reduced TiO_2 as highly efficient catalyst for hydrogen evolution

Li-Na Chen,[a] Su-Heng Wang,[a] Peng-Yang Zhang,[a] Zhi-Xin Chen,[a] Xiao Lin,[b] Hui-Juan Yang,[c] Tian Sheng,*[d] Wen-Feng Lin*[e], Na Tian,[a] Shi-Gang Sun[a], and Zhi-You Zhou*[a]

[a] State Key Laboratory for Physical Chemistry of Solid Surfaces, Collaborative Innovation Center of Chemistry for Energy Materials, College of Chemistry and Chemical Engineering, Xiamen University, Xiamen, 361005, China.

[b] Department of Chemical Engineering and Biotechnology, University of Cambridge, Cambridge, CB3 0AS, UK.

[c] Institute of Advanced Electrochemical Energy, School of Materials Science and Engineering, Xi'an University of Technology, Xi'an 710048, China

[d] College of Chemistry and Materials Science, Anhui Normal University, Wuhu, 241000, China.

[e] Department of Chemical Engineering, Loughborough University, Loughborough, Leicestershire LE11 3TU, UK.

ABSTRACT. The development of low-cost yet highly efficient catalysts for hydrogen evolution reaction (HER) is crucial for large-scale clean and sustainable hydrogen production from water splitting. Tuning the interfacial structure of catalyst has emerged as an effective strategy to optimize the intrinsic catalytic activity. In this study, we demonstrated the deposition of Ru nanoparticles by freshly prepared strong reductive Ti(III) oxide, resulting in Ru/reduced TiO_2 interface with oxygen vacancies. The as-prepared Ru/r-TiO_2 exhibited a superior HER performance over commercial Pt/C in alkaline media, only with a small overpotential of 15 mV required to deliver the benchmark current density of 10 mA cm^{-2} and a high turnover frequency of 8.74 s^{-1} at an overpotential of 100 mV. Density functional theory calculation indicates that high electrocatalytic activity of Ru/r-TiO_2 is originated from the promotion of water dissociation and weakening OH adsorption by reduced TiO_2, which facilitates the conversion of water to H_2. This work provides an efficient strategy for the design of high-performance HER catalysts.

KEYWORDS: *Hydrogen evolution, Ru-based Electrocatalyst, Oxygen vacancy, Reduced TiO_2, Interfacial structure*

Graphical Abstract

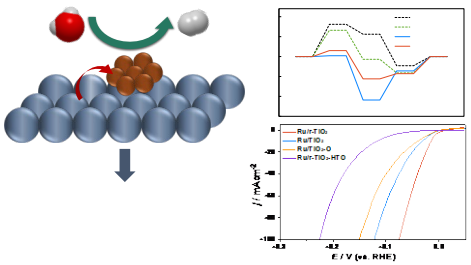

1. Introduction

Hydrogen has been proposed as an ideal next-generation fuel to provide clean and sustainable energy via fuel cells [1, 2]. Electrochemical water splitting is a promising approach to substitute steam reforming for low-carbon H_2 production, which is a renewable and environmentally friendly route to generate high pure H_2 for fuel cells [3-7]. Water electrolysis can be performed in both acidic and alkaline electrolytes. In acidic media, hydrogen evolution reaction (HER) at cathode is facile, however, oxygen evolution reaction (OER) at anode is very sluggish and it is a great challenge to find an efficient and stable catalyst. By contrast, in alkaline media, the OER is much improved and allows the use of low-cost transitional metal-based catalysts, but the HER becomes a problem, as its reaction rate is 2-3 orders of magnitude lower than that in the acidic media for Pt-based catalysts [8-12]. Therefore, the rational design the highly efficient HER catalysts in alkaline media is of great importance [13]. Generally, electrocatalytic reactions occur on the interface of electrocatalysts, which greatly influences the energy barrier of reaction intermediates [14, 15]. Thus, modulating the interfacial structure of the electrocatalysts is an effective way to optimize the HER performance [16].

Among various ways for interfacial structure modulation for HER catalysts, constructing metal/oxide interfaces have been demonstrated as a promising strategy to optimize the HER electrocatalysts, including electrocatalytic activity and stability [17-20]. The alkaline HER process involves the water dissociation to adsorbed H* and OH*, and the recombination of H* to H_2, as well as the desorption of OH*. Currently, most of efforts have been focused on the improvement of water dissociation and/or H* adsorption [17, 21, 22]. For example, the introduction of 3d transition metal oxides/hydroxides on the Pt surfaces can greatly boost the

alkaline HER through the acceleration of water dissociation [17]. Nonetheless, an optical HER electrocatalyst requires a balance between facilitating water dissociation and preventing the 'poisoning' by OH* [17, 18]. However, little attention has been paid to the rational modulation of OH* desorption. Previous work reported that oxygen vacancies in metal oxide can greatly influence the interaction of metal/oxide interfaces, and thus tune the adsorption and desorption of the intermediates [23-26]. Therefore, exploring the impact of oxygen vacancies on OH* desorption in alkaline HER is promising.

Herein, we proposed a facile strategy to construct metal/oxide catalyst by introducing a strong reductive Ti(III) oxide as the support of Ru nanocatalyst to *in-situ* deposit Ru nanoparticles anchored on partially reduced rutile TiO_2 (denoted as Ru/r-TiO_2). The as-prepared catalyst obtained abundant oxygen vacancies and strong interaction between metal and support, as indicating the existence of negatively charged Ru. This is a mild method to introduce strong metal-support interaction without high-temperature reduction/oxidation [27-29]. The Ru/r-TiO_2 exhibited an excellent alkaline HER activity, reaching the benchmark current density of 10 mA cm^{-2} only at a small overpotential of 15 mV, and a high turnover frequency (TOF) of 8.74 s^{-1} at an overpotential of 100 mV. This performance is much superior to those of control Ru-based samples without oxygen vacancies, as well as the commercial Pt/C catalyst. Density functional theory (DFT) calculations reveal that reduced TiO_2 with oxygen vacancies facilitates both the water dissociation and weakening OH adsorption, resulting in the excellent electrocatalytic activity of Ru/r-TiO_2.

2. Experimental section

2.1 Preparation of Ru-based catalysts

Synthesis of Ti(III) oxide. In Ar atmosphere, 0.25 g $TiCl_3$, 0.35 g NaCl and 1 mL ultra-pure water were added into a Schlenk bottle, stir for 12 h at 100 ℃ to get blue Ti(III) oxide precipitation [30]. The obtained Ti(III) oxide had the poor crystallinity (Fig. S1).

Synthesis of Ru/r-TiO_2. Adding 40 mg $RuCl_3$ into the separating Ti(III) oxide at 80 ℃ in Ar atmosphere, after mixing evenly for 30 min, excessive $NaBH_4$ was added into the mixture and stir for 6 h. $RuCl_3$ was hardly reduced completely by Ti(III) oxide due to slow reduction kinetics. Adding $NaBH_4$ can completely reduce the residual $RuCl_3$ to Ru nanoparticles anchored on the reduced support. The resulting black powder was washed by ultra-pure water and collected by centrifugation for 3 times. Finally, the black powder was dried at 60 ℃ in vacuum oven, and then grinded into fine powder to get Ru/r-TiO_2 catalyst.

Synthesis of Ru/TiO_2 and Ru/TiO_2-O. Adding 1 mL ultra-pure water into separating Ti(III) oxide and stir in air for 24 h to get TiO_2 solid. The following experiments of depositing Ru nanoparticles on Ti oxide were the same with the above synthesis of Ru/r-TiO_2 catalyst. In this step, the atmosphere in Ar is to get Ru/TiO_2 catalyst and in air is to get Ru/TiO_2-O catalyst.

Synthesis of Ru/r-TiO_2-HTO. The obtained Ru/r-TiO_2 catalyst was heated in air at 700 K for 15 min to get Ru/r-TiO_2-HTO catalyst.

2.2 Catalyst Characterizations

Transmission electron microscopy (TEM), scanning transmission electron microscopy (STEM) images, and elemental mapping analysis were performed using a Philips Tecnai F30 at 300 kV. Powder X-ray diffraction (XRD) was performed on Panalytical X'pert PRO X-ray

diffractometer with monochromated Cu Kα radiation (40 kV, 30 mA). Inductively coupled plasma atomic mass spectrometry (ICP-MS) measurements were performed on PerkinElmer. X-ray photoelectron spectroscopy **(**XPS) was carried out on PHI5000VPIII hemispherical electron energy analyzer with monochromatized Al Kα radiation (1,486.6 eV). Electron paramagnetic resonance (EPR) was performed at Bruker EMX-10/12 with the temperature at 90 K.

2.3 Electrochemical measurement

To prepare catalyst ink, Ru/r-TiO_2 (1.0 mg) and XC-72 carbon black (1.0 mg) were ultrasonically dispersed in a mixture of water (0.50 mL), ethanol (0.50 mL) and 5% Nafion (15 μL) for 1 h. The 25 μL of ink was pipetted onto a glassy carbon (GC, ϕ = 5 mm) disk electrode, resulting in a catalyst loading of 37 μg_{Ru} cm^{-2}. The introduction of carbon black into catalyst ink could improve the electronic conductivity and the dispersion of the catalyst on the electrode surface. The electrodes of Ru/TiO_2, Ru/TiO_2-O and Ru/r-TiO_2-HTO were prepared as the same procedure. Commercial Pt/C (20 wt%, Johnson Matthey) was used as benchmark material, and the Pt loading on the GC electrode was also 37 μg_{Pt} cm^{-2}.

HER activity was tested in H_2-saturated 0.1 M KOH solution at 30 ^oC on a rotating disk electrode (RDE) system (Pine Inc.) with a CHI-760E bipotentiostat. A glassy carbon plate was used as counter electrode, and a Hg/HgO was used as reference electrode. All potentials were reported versus the reversible hydrogen electrode (RHE) scale. HER polarization curves of all the catalysts in this study were recorded through staircase voltammetry at an equivalent rate of 5 mV s^{-1}, and corrected by solution ohmic drop. The electrode rotating rate was 1600 rpm to improve mass transfer and alleviate the blocking effect of H_2 bubble on the electrode surface.

Electrochemical impedance spectroscopy (EIS) measurements were carried out on a Parstat 2263 potentiostat in the frequency range of 100 kHz–0.1 Hz with AC amplitude of 5 mV.

2.4 DFT calculations

All electronic structure calculations were carried out using the VASP with Perdew−Burke−Ernzerhof (PBE) functional of exchange-correlation. The projector-augmented-wave (PAW) pseudopotentials were utilized to describe the core-valence electron interaction with electrons from Ti 3p, 3d, 4s; O 2s, 2p; and H 1s shells [31-35]. The on-site Hubbard U term (DFT+ U) was added on O 2p orbitals at the value of 6.3 eV [36]. The cutoff energy was set to 450 eV. The vacuum height in the z direction was above 12 Å. The Ru(0001) and Pt(111) surfaces were modeled as a *p*(2×2) periodic slab with five layers with 20 Ru(Pt) atoms. The bottom two layers were fixed and other atoms were relaxed. A 6×6×1 Monkhorst-Pack *k*-point sampling was used. The rutile TiO_2(110) surface was modeled as a *p*(2×3) periodic slab with three layers with 36 Ti and 72 O atoms. The bottom one layer was fixed and other atoms including supported Ru atoms were relaxed during geometry optimizations. The five-layer Ru(0001) surface with 40 atoms was placed above on TiO_2(110) to model the Ru/TiO_2 interface for investigating the adsorption and dissociation of water at the interface. For simulating the reduced TiO_2(110) surface, two rows of bridge oxygen atoms were removed. A 6×1×1 Monkhorst-Pack *k*-point sampling was used for the TiO_2-supported models. The adsorption energy was defined in this work as: E_{ad} = E(ad/surf) - E(surf) - E(ad), where E(w/surf), E(w), and E(surf) are the total energies of the adsorbate binding to surface, free adsorbate in gas phase and clean surface, respectively. The free energy of species was obtained from G = E + ZPE - TS, where E is the total energy of species, S is the entropy and ZPE is the zero-point energy at 300

K. All the vibrational frequencies, v_i (Hz), were calculated based on the harmonic oscillators approximation [37]. The charge transfer was analyzed by Bader method.

3. Results and discussions

3.1 Characterization of morphology and structure.

Fig. 1a illustrates the preparation of Ru nanoparticles anchored on partially reduced TiO_2 and normal TiO_2 catalysts under Ar atmosphere, i.e., Ru/r-TiO_2 and Ru/TiO_2. The Ru weight contents were about 30% (Table S1), determined by the inductively coupled plasma mass spectrometry (ICP-MS) with the NaClO as the digestion solution [38]. Fig. 1b shows the XRD of the as-prepared Ru/r-TiO_2. The indicated peaks can be indexed to the rutile TiO_2 (PCPDF no. 21-1276) and hexagonal Ru (PCPDF no. 060663). TEM images revealed that Ru nanoparticles with average size of 2.1 nm were homogeneously distributed on the TiO_2 support (Fig. 1c). Some Ru nanoparticles with a lattice space of 0.214 nm, corresponding to hexagonal Ru (002) plane[39], can be observed in the HRTEM image (Fig. S2). The crystal structure with lattice space of 0.324 nm was clearly visible (inset of Fig. 1c), which was attributed to the (110) plane of rutile TiO_2. This result indicated that most of Ti(III) oxide had been converted into TiO_2 on the sample of Ru/r-TiO_2. The formation of TiO_2 may be caused by the $RuCl_3$ oxidation and inevitable exposure to air or dissolved O_2 during washing and centrifugation steps in the synthesized process, as well as in the characterization and test process. The annular dark-field (ADF-STEM) coupled with energy-dispersive X-ray spectroscopy (EDX) element mapping images indicated that the homogeneous distribution of the element Ru, Ti, and O over the entire area (Fig. 1d). The control samples, i.e., Ru/TiO_2, Ru/TiO_2-O and Ru/r-TiO_2-HTO, showed similar morphologies, the

crystal structure of TiO_2, and Ru particle sizes as Ru/r-TiO_2 (Fig. S3), which is favorable for the comparison of HER performance.

XPS was employed to investigate the near-surface charge state of these samples (Fig. 2 and Fig. S4). The Ru 3d spectra clearly exhibited that binding energies of Ru decreased in the order of Ru/r-TiO_2 < Ru/TiO_2 < Ru/TiO_2-O < Ru/r-TiO_2-HTO (Fig. 2a). The same trend was also observed in Ru 3p spectra (Fig. S4b). Among these samples, the Ru/r-TiO_2 had the lowest binding energy, indicating the highest electron density on Ru. To get an insight into the charge state of Ru in Ru/r-TiO_2, Ru 3d spectra were deconvoluted into three doublet peaks of Ru $3d_{5/2}$ and $3d_{3/2}$ with confined conditions of spin-orbit splitting distance of 4.1 eV and area ratio of 3:2, [40] as well as one carbon contamination at 284.27 eV, as shown in Fig. 2b and Table S2. For the sake of comparison, the Ru 3d XPS of metal Ru black and RuO_2/TiO_2 were also tested, and the binding energies of Ru $3d_{5/2}$ were at 280.00 and 281.1 eV, respectively (Fig. S4d). Therefore, three Ru 3d5/2 peaks of Ru/r-TiO2 at 279.35, 279.98, and 280.98 eV can be assigned to negatively charged Ru, metallic Ru, and oxidized Ru [41, 42]. The existence of negatively charged Ru with lower binding energy than metal Ru implies the significant electron transfer from the reduced TiO_2 support to Ru nanoparticles on the Ru/r-TiO_2 due to the strong metal-support interaction. In contrast, only metallic Ru and oxidized Ru species could be observed on the Ru/TiO_2, Ru/TiO_2-O, and Ru/r-TiO_2-HTO (Fig. 2b and Fig. S4).

Furthermore, high-resolution XPS Ti 2p spectra were collected to clarify the Ti environment in Ru/r-TiO_2 (Fig. 2c). The peaks at 458.44 and 464.18 eV were assigned to Ti $2p_{3/2}$ and $2p_{1/2}$, respectively. The peak located at 461.66 eV between Ti $2p_{3/2}$ and $2p_{1/2}$ was contributed to the Ru $3p_{3/2}$. Compared with Ru/TiO_2, Ru/r-TiO_2 exhibited negatively shifted binding energies of 0.51 eV for Ru $3p_{3/2}$, and 0.37 eV for Ti 2p (Fig. 2c). In addition, the Ti 2p spectra clearly

show that the binding energy of Ti follows the order: Ru/r-TiO_2 < Ru/TiO_2 < Ru/TiO_2-O < Ru/r-TiO_2-HTO (Fig. S4g). The shift toward lower binding energy in Ti 2p indicates the fewer O neighbors around the Ti on average, which suggests the existence of oxygen vacancies in Ru/r-TiO_2 [43]. To clarify the oxygen vacancies in Ru/r-TiO_2 more clearly, electron paramagnetic resonance (EPR) was employed, because this method is sensitive to paramagnetic species containing unpaired electrons, such as Ti^{3+} and oxygen vacancies, but silence to TiO_2 [44, 45]. As shown in Fig. 2d and Fig. S5, obvious EPR peak was observed on Ru/r-TiO_2. The EPR signals at $g_{\perp}$ = 1.9627 and $g_{\parallel}$ = 1.9383 are assigned to the surface Ti^{3+} with oxygen vacancies [46, 47]. No obvious EPR signals could be observed on Ru/TiO_2, Ru/TiO_2-O, and Ru/r-TiO_2-HTO (Fig. 2d and Fig. S5). Overall, the above results confirm that introducing the Ti(III) oxide as support successfully tailored negatively charged Ru nanoparticles supported on partially reduced TiO_2 and the strong interaction between Ru and Ti oxide makes it possible to stabilize oxygen vacancies on the interface in Ru/r-TiO_2. In addition, oxygen defects can usually increase the electrical conductivity of TiO_2, which may facilitate the electron transfer from the Ru nanoparticles to the support.

2.2 Electrocatalytic activity and stability towards HER

Electrocatalytic HER performance was tested through steady-state linear sweep voltammetry (LSV) in H_2-saturated 1.0 M KOH. For better comparison, similar noble metal loading (Ru or Pt loading around 37 μg cm^{-2}) on the electrode was applied for all electrocatalysts studied. Fig. 3a shows the HER polarization curves of Ru/r-TiO_2, Ru/TiO_2, commercial Pt/C and Ru/C, as well as Ti(III) oxide, TiO_2 and bare GC electrode in H_2-saturated 1.0 M KOH solution. The control samples of Ti(III) oxide, TiO_2, and bare GC electrode without

noble metals show the negligible HER performance in alkaline media. For the Ru/r-TiO_2, it just needed -15 mV overpotential to reach a benchmark current density of 10 mA cm^{-2}. This is considerably better than Ru/TiO_2 (-32 mV) and Pt/C (-34 mV), and also better than recently reported Ru@C_2N (-17 mV) [39], RuCoP (-23 mV) [48], and other non-platinum electrocatalysts (Table S3). At the current density higher than 10 mA cm^{-2}, Ru/r-TiO_2 also exhibited the superior HER catalytic activity with the overpotential of 25 mV at 20 mA cm^{-2}, and 76 mV at 100 mA cm^{-2} (Fig. 3b). By comparing with the control samples in Fig. 3c, Ru/r-TiO_2 exhibited a much better HER activity than Ru/TiO_2, Ru/TiO_2-O and Ru/r-TiO_2-HTO, for the latter cases, the overpotentials for current density at 10 mA cm^{-2} were 32, 41, and 117 mV, respectively. Heat treatment of Ru/r-TiO2 catalyst at 573 K in inert Ar atmosphere, which may increase the crystallinity and conductivity of TiO2, can further slight improve the HER activity (Fig. S6).

Moreover, we found Ru/TiO_2 also exhibited higher HER activity than commercial Pt/C and Ru/C, indicating a positive impact from the TiO_2 support. Typically, the alkaline HER process involves the initial water adsorption and dissociation to yield adsorbed H* and OH* (Volmer step). An optimal electrocatalyst requires a balance between facilitating water dissociation and preventing 'poisoning' with OH* [17, 18]. Previously, Markovic's group found that the introduction of $Ni(OH)_2$ nanoclusters on Pt can greatly boost alkaline HER activity and proposed the critical role of water dissociation [17]. Therefore, the improvement of alkaline HER activity in Ru/TiO_2 observed here may also be caused by TiO_2 for the enhancement of water dissociation. Due to the existence of TiO_2 in both Ru/r-TiO_2 and Ru/TiO_2 electrocatalysts, so that the different HER activity between them could not be attributed to the promotion of water dissociation by TiO_2 solely.

To better understand the electrocatalytic mechanism of Ru/r-TiO_2, the Tafel slope (Fig. 3d) was investigated. Tafel slope of Ru/r-TiO_2 (49 mV dec^{-1}) was significantly lower than those of the control samples, e.g., Pt/C (54 mV dec^{-1}), Ru/TiO_2 (60 mV dec^{-1}), Ru/TiO_2-O (80 mV dec^{-1}), Ru/r-TiO_2-HTO (95 mV dec^{-1}), and Ru/C (84 mV dec^{-1}), which confirms the more favorable HER kinetics on Ru/r-TiO_2. At the higher current density (> 80 mA cm^{-2}), the Tafel slope of Ru/r-TiO_2 increased to 123 mV dec^{-1} (Fig. S7). As for HER via Volmer-Heyrovsky mechanism, the theoretical Tafel slopes are 40 and 120 mV dec^{-1} at low and high current density, respectively [49]. Therefore, the HER on Ru/r-TiO_2 is via the Volmer-Heyrovsky mechanism and the Heyrovsky step is the rate determine step [49]. To further reveal the electrocatalytic kinetics, the electrochemical impendence measurement was implemented. The Nyquist plots of those electrocatalysts at the overpotential of 50 mV are shown in Fig. S8. The Nyquist plots show just one semicircle, which indicates a single time constant for all results. The smaller semi-circular diameter in the electrochemical impedance spectrum of Ru/r-TiO_2 indicates its faster charge transfer, which leads to the improvement of HER performance. The extremely low activity of Ru/r-TiO_2-HTO, even inferior to Ru/C, is unanticipated. This sample was prepared by high-temperature (700 K) oxidation treatment of Ru/r-TiO_2 in air, and the binding energy of Ru $3d_{5/2}$ (i.e., Ru-2 species in Fig. 2b) was 280.71 eV, considerably higher than that of metallic Ru (280.00 eV), as shown in Fig. 2 and Table S2. Thus, this unfavorable change of the electronic structure may lead to the poor HER activity of the Ru/r-TiO_2-HTO.

To evaluate the intrinsic activity of electrocatalyst, TOF was measured. The numbers of active sites were evaluated by underpotential deposition (UPD) of Cu on Ru (Fig. S9) [50, 51]. The TOF values at the overpotential of 25, 50, and 100 mV were summarized and compared in Fig. 3e. The TOF values of Ru/r-TiO_2 at the overpotential of 25, 50, and 100 mV are 1.08, 2.98,

and 8.74 s^{-1}, respectively, which are considerably higher than the Pt/C (0.52 s^{-1} @25 mV, and 1.57 s^{-1} @50 mV) in this study, and those of other reported electrocatalysts (Table S4), such as Pt/C(1.7 s^{-1} @100 mV) [52], Ru@C_2N (0.76 s^{-1} @25mV) [39], RuCoP (7.26 s^{-1} @100mV) [48], and Ru/C_3N_4/C (4.2 s^{-1} @100 mV) [52]. Furthermore, the TOF of Ru/r-TiO_2 is about 3.5 times larger than that of Ru/TiO_2 (0.30 s^{-1} @25mV). The stability of Ru/r-TiO_2 was further tested according to the previously reported methods [53, 54]. After 1000 potential cycles, there is essentially no change in the polarization curves (Fig. 3f). At a fixed overpotential of 0.015 V, the Ru/r-TiO_2 just exhibited slight degradation of HER activity over 10 h (inset of Fig. 3f), indicating a good stability of Ru/r-TiO_2. To investigate the structure change, we measured the XPS and EPR of Ru/r-TiO_2 after HER test. The Ru 3d spectrum showed no change in binding energy, and Ti 2p was slight shifted to low binding energy (Fig. S10). EPR shows more obvious change than the XPS. As shown in Fig. S11, there are two EPS signals. One comes from surface Ti^{3+} with oxygen vacancies as the initial Ru/r-TiO_2, but the band intensity is weakened considerably. The other one is at g = 2.0021, assigned to the hole trapped on the bulk rutile TiO_2 [46, 47], and it might be caused by the electroreduction of TiO_2 during the HER process. The above structure change, especially the attenuation of surface Ti^{3+} with oxygen vacancies, may result in the degradation of HER performance of Ru/r-TiO_2.

2.3 DFT calculations for mechanism of enhanced HER on Ru/r-TiO_2.

To elucidate the impact of the Ru nanoparticles supported on partially reduced TiO_2 to boost the alkaline HER, we carried out DFT calculations. On basis of XRD and HRTEM results, thin layer Ru(0001) and rutile TiO_2(110) with and without surface oxygen vacancy were employed as models for Ru(0001)/r-TiO_2 and Ru(0001)/TiO_2, respectively. For the structure of Ru(0001)/TiO_2, the five-layered Ru(0001) was located on the three-layered pristine TiO_2(110)

surface (Fig. S12). For simulating the reduced TiO_2(110) surface, two rows of bridge oxygen atoms were removed, as shown in Fig. S12. It can be seen that the 0.67 ML surface bridge oxygen atoms were removed, leaving 0.33 ML bridge oxygen atoms. The dashed orange cycles indicate the position of the removed two rows of bridge oxygen atoms with the direct binding between Ti atoms and Ru clusters. The calculated ZPE and TS for intermediates was listed in Table S5. The oxygen defect formation energy of the reduced TiO_2 surface was 3.88 eV, which was defined: $E_d = E(def) + E(H_2O) - E(surf) - E(H_2)$, where E(def) and E(surf) are the total energies of reduced TiO_2 and pristine TiO_2, $E(H_2O)$ and $E(H_2)$ are the free energies of H_2 and H_2O in gas phase at 300 K. The adhesion energy of the Ru cluster was calculated to be -5.16 eV on pristine TiO_2(110) and -8.79 eV on reduced TiO_2(110), indicating that the Ru cluster on the reduced surface is more thermodynamically stable [55]. The water effect was not considered in this study, however we found it may be negligible in energetics for the Volmer step (Fig. S13).

As shown in Fig. 4a, for the Ru(0001)/TiO_2, electron (-2.42 q) transfer from Ru cluster to the pristine TiO_2(110) was found, resulting in the positively charged Ru cluster. By contrast, for the Ru(0001)/r-TiO_2, the opposite electron (-0.31 q) transfer from the partially reduced TiO_2(110) to the Ru cluster occurred, leading to the negatively charged Ru. These data are in good agreement with the experimental results (Fig. 2).

In alkaline medium, HER generally possesses Volmer-Heyrovsky or Volmer-Tafel two steps:

Volmer step: $H_2O + * + e^- \rightarrow H^* + OH^-$

Heyrovsky step: $H_2O + H^* + e^- \rightarrow H_2 + M + OH^-$

Tafel step: $2H^* \rightarrow H_2$

The initial Volmer step is water dissociation to yield H* and OH*, and followed by Heyrovsky or Tafel step to generate H_2 [56]. The free energy profiles for HER, i.e., from water to H_2, on Ru(0001)/ TiO_2 and Ru(0001)/r-TiO_2, as well as the benchmarks of pristine Ru(0001) and Pt(111), are shown in Fig. 4b. The identified key intermediates and transition states on Ru(0001)/r-TiO_2 and Ru(0001)/TiO_2 are presented in Fig. 4c. We first discussed the kinetics of water dissociation in alkaline media. The energy barriers of O-H bond breaking of water on the pristine Pt(111) and Ru(0001) surfaces were calculated to be 0.81 and 0.66 eV, respectively, which suggested that water dissociation on pure Pt or Ru was quite slow. However, on the Ru(0001)/TiO_2 and Ru(0001)/r-TiO_2 interfaces, the water molecule could readily adsorb onto the Ti sites of TiO_2(110) or r-TiO_2(110) surfaces and then transfer the H* to the supported Ru clusters, as shown in Fig. 4b and 4c, with a tiny barrier of 0.02 eV at the Ru(0001)/TiO_2 interface and a very small barrier of 0.15 eV at the Ru(0001)/r-TiO_2 interface, strongly indicating that the water dissociation kinetics was much facilitated by TiO_2 or r-TiO_2. This promotion effect by TiO_2 is consistent with 3d M(Ni, Co, Fe, and Mn) hydr(oxy)oxide on Pt as reported previously [17, 18].

An excellent alkaline HER electrocatalyst needs a balance between water dissociation and OH* desorption;[31] too strong adsorption of OH* can poison the surface. The Tafel slopes of Ru/r-TiO_2 and Ru/TiO_2 are 49 and 60 mV dec^{-1}, respectively, which suggests that HER is via the Volmer-Heyrovsky mechanism. The H* adsorption of Ru(0001)/r-TiO_2 surface (-0.43 eV) is marginally stronger than that of Ru(0001)/TiO_2 surface (-0.36 eV), as shown in Fig. 4c. Such a slight difference in the H* adsorption energy can be negligible. In the view of energetics, the adsorption energy of H* is negative. The desorption of two H* by Tafel mechanism is not thermodynamically feasible than that by Heyrovsky mechanism.

Very interestingly, the OH* desorption has a great difference between Ru(0001)/TiO_2 and Ru(0001)/r-TiO_2 interface. The change in free energy of OH* desorption on Ru(0001)/TiO_2 is 0.73 eV, which is much higher than that on the Ru(0001)/r-TiO_2 interface (0.11 eV). This implies that the OH* can strongly adsorbed on Ru(0001)/TiO_2 interface and deactivate the Ti sites for further water dissociation. In contrast, the remarkably weakened OH* adsorption at Ru(0001)/r-TiO_2 can facilitate the OH* desorption to free up the Ti sites for continuing turning over water to H* and finally H_2, which might attribute to the existence of oxygen vacancies on Ru(0001)/r-TiO_2 interface.

To figure out the relationship between OH* adsorption and oxygen vacancies at Ru(0001)/r-TiO_2 interface, the adsorption structure of OH* was analyzed. As shown in Fig. 4d and 4e, the OH* structure at Ru(0001)/r-TiO_2 with oxygen vacancies is quite different from that at the Ru(0001)/TiO_2 interface without oxygen vacancies. As for OH* adsorbed at the Ru(0001)/r-TiO_2 interface, the distance Ru and O is 3.17 Å (Fig. 4d), which is far beyond Ru-O single bond. That is, OH* only binds with Ti site. While the OH* is quite close to Ru sites at the Ru(0001)/TiO_2 interface, and the Ru-O distance is 2.20 Å (Fig. 4e), which is in the range of Ru-O single bond [57, 58]. That is, OH* binds with both Ti and Ru sites. The desorption of OH* from Ru(0001)/TiO_2 interface needs to overcome additional bond strength of Ru-O, thus increasing the desorption energy barrier. The existence of oxygen vacancies at Ru(0001)/r-TiO_2 interface may significantly change the local electronic structure to mediate the interaction between TiO_2 and Ru, thus facilitating the OH* desorption from Ti sites. In addition, the negatively charged Ru site generated from electronic interaction between Ru and TiO_2 with oxygen vacancies may repel the OH* and weaken its adsorption.

The above DFT calculations indicate that although pristine TiO_2 can promote the water dissociation to H* and OH*, too strong adsorption of OH* bound with both Ru and Ti sites at the Ru(0001)/TiO_2 interface, is unfavorable for HER due to the difficulty in OH* desorption. On the TiO_2 with surface oxygen vacancies, OH* is only bound with Ti site and can be desorbed easily. The combination of promoting water dissociation with weakening OH* adsorption results in the excellent HER electrocatalytic activity of Ru/r-TiO_2.

4. Conclusions

In summary, a facile approach to fabricate Ru nanoparticles anchored on partially reduced rutile TiO_2 has been developed, by employing a freshly prepared strong reductive Ti(III) oxide as the support to deposit Ru nanocatalyst. The as-prepared Ru/r-TiO_2 nanocomposite catalyst exhibited a superior performance towards hydrogen evolution reaction (HER) in alkaline media, with only a small overpotential of 15 mV required to deliver a benchmark current density of 10 mA cm^{-2}, as well as an exceptionally high turnover frequency of 8.74 s^{-1} at an overpotential of 100 mV, which is much better than that of control samples without Ti(III) oxide as a support source and also commercial Pt/C. DFT calculations indicate that the excellent HER performance of Ru/r-TiO_2 in the alkaline medium can be attributed that r-TiO_2 can promote the water dissociation kinetics to yield H* and OH*, and the existence of oxygen vacancies on the r-TiO_2 will weaken OH* adsorption, and promote its desorption to free up Ti sites for continuing water dissociation and hydrogen production. Quantitative correlation of the surface oxygen vacancies with OH* adsorption energy and HER catalytic activity is needed in future studies.

Corresponding Authors

* Email: zhouzy@xmu.edu.cn; tsheng@ahnu.edu.cn; w.lin@lboro.ac.uk

Declaration of Competing Interest

The authors declare that they have no known competing financial interests or personal relationships that could have appeared to influence the work reported in this paper.

Acknowledgements

This work was financially supported by grants from National Key Research and Development Program of China (2020YFB1505804), National Natural Science Foundation of China (21875194, 92045302, 21903001, and 22021001), Minister of Science and Technology of China (through the high-level foreign expert program, G20190013008), the EPSRC (EP/I013229/1) and the Royal Society via the Newton Fund (NAF\R1\191294).

Appendix A. Supporting Information

Supplementary data associated with this article can be found in the online version at doi:10.1016/j.nanoen.xxxx.xxxxxx.

References

[1] J.O.M. Bockris, The origin of ideas on a Hydrogen Economy and its solution to the decay of the environment, Int. J. Hydrogen Energy, 27 (2002) 731-740.
[2] N.S. Lewis, D.G. Nocera, Powering the planet: Chemical challenges in solar energy utilization, Proc. Nat. Acad. Sci., 103 (2006) 15729-15735.
[3] C.G. Morales-Guio, L.-A. Stern, X. Hu, Nanostructured hydrotreating catalysts for electrochemical hydrogen evolution, Chem. Soc. Rev., 43 (2014) 6555-6569.
[4] I. Roger, M.A. Shipman, M.D. Symes, Earth-abundant catalysts for electrochemical and photoelectrochemical water splitting, Nat. Rev. Chem., 1 (2017) 0003.
[5] Z. Chen, T. Wang, T. Sun, Z. Chen, T. Sheng, Y.-H. Hong, Z.-A. Nan, J. Zhu, Z.-Y. Zhou, H. Xia, S.-G. Sun, Nickel Complexes with Non-innocent Ligands as Highly Active Electrocatalysts for Hydrogen Evolution, Chin. J. Chem . 36 (2018) 1161-1164.
[6] X. Gao, Y.-j. Gao, S.-q. Li, J. Yang, G.-l. Zhuang, S.-w. Deng, Z.-H. Yao, X. Zhong, Z.-z. Wei, J.-g. Wang, Defect CTF derived Ru-based catalysts for high performance overall water splitting reaction, J. Energy Chem., 50 (2020) 135-142.

[7] K. Li, Y. Li, Y. Wang, J. Ge, C. Liu, W. Xing, Enhanced electrocatalytic performance for the hydrogen evolution reaction through surface enrichment of platinum nanoclusters alloying with ruthenium in situ embedded in carbon, Energy Environ. Sci., 11 (2018) 1232-1239.
[8] W. Sheng, H.A. Gasteiger, Y. Shao-Horn, Hydrogen Oxidation and Evolution Reaction Kinetics on Platinum: Acid vs Alkaline Electrolytes, J. Electrochem. Soc., 157 (2010) B1529-B1536.
[9] J. Durst, A. Siebel, C. Simon, F. Hasché, J. Herranz, H.A. Gasteiger, New insights into the electrochemical hydrogen oxidation and evolution reaction mechanism, Energy Environ. Sci., 7 (2014) 2255-2260.
[10] H. Jin, X. Liu, S. Chen, A. Vasileff, L. Li, Y. Jiao, L. Song, Y. Zheng, S.-Z. Qiao, Heteroatom-Doped Transition Metal Electrocatalysts for Hydrogen Evolution Reaction, ACS Energy Lett., 4 (2019) 805-810.
[11] P. Yu, F. Wang, T.A. Shifa, X. Zhan, X. Lou, F. Xia, J. He, Earth abundant materials beyond transition metal dichalcogenides: A focus on electrocatalyzing hydrogen evolution reaction, Nano Energy, 58 (2019) 244-276.
[12] Q. Jin, B. Ren, D. Li, H. Cui, C. Wang, In situ promoting water dissociation kinetic of Co based electrocatalyst for unprecedentedly enhanced hydrogen evolution reaction in alkaline media, Nano Energy, 49 (2018) 14-22.
[13] Z.W. Seh, J. Kibsgaard, C.F. Dickens, I. Chorkendorff, J.K. Nørskov, T.F. Jaramillo, Combining theory and experiment in electrocatalysis: Insights into materials design, Science, 355 (2017) eaad4998.
[14] N.M. Markovic, Interfacing electrochemistry, Nat. Mater., 12 (2013) 101-102.
[15] V.R. Stamenkovic, D. Strmcnik, P.P. Lopes, N.M. Markovic, Energy and fuels from electrochemical interfaces, Nat. Mater., 16 (2017) 57-69.
[16] Q. Shao, P. Wang, X. Huang, Opportunities and Challenges of Interface Engineering in Bimetallic Nanostructure for Enhanced Electrocatalysis, Adv. Funct. Mater., 29 (2019) 1806419.
[17] R. Subbaraman, D. Tripkovic, D. Strmcnik, K.-C. Chang, M. Uchimura, A.P. Paulikas, V. Stamenkovic, N.M. Markovic, Enhancing Hydrogen Evolution Activity in Water Splitting by Tailoring Li+-Ni(OH)2-Pt Interfaces, Science, 334 (2011) 1256-1260.
[18] R. Subbaraman, D. Tripkovic, K.-C. Chang, D. Strmcnik, A.P. Paulikas, P. Hirunsit, M. Chan, J. Greeley, V. Stamenkovic, N.M. Markovic, Trends in activity for the water electrolyser reactions on 3d M(Ni,Co,Fe,Mn) hydr(oxy)oxide catalysts, Nat. Mater., 11 (2012) 550-557.
[19] P. Wang, K. Jiang, G. Wang, J. Yao, X. Huang, Phase and Interface Engineering of Platinum–Nickel Nanowires for Efficient Electrochemical Hydrogen Evolution, Angew. Chem. Int. Ed., 55 (2016) 12859-12863.
[20] Z. Zhao, H. Liu, W. Gao, W. Xue, Z. Liu, J. Huang, X. Pan, Y. Huang, Surface-Engineered PtNi-O Nanostructure with Record-High Performance for Electrocatalytic Hydrogen Evolution Reaction, J. Am. Chem. Soc., 140 (2018) 9046-9050.
[21] N. Mahmood, Y. Yao, J.-W. Zhang, L. Pan, X. Zhang, J.-J. Zou, Electrocatalysts for Hydrogen Evolution in Alkaline Electrolytes: Mechanisms, Challenges, and Prospective Solutions, Adv. Sci., 5 (2018) 1700464.
[22] P. Wang, X. Zhang, J. Zhang, S. Wan, S. Guo, G. Lu, J. Yao, X. Huang, Precise tuning in platinum-nickel/nickel sulfide interface nanowires for synergistic hydrogen evolution catalysis, Nat. Commun., 8 (2017) 14580.

[23] R. Schaub, P. Thostrup, N. Lopez, E. Lægsgaard, I. Stensgaard, J.K. Nørskov, F. Besenbacher, Oxygen Vacancies as Active Sites for Water Dissociation on Rutile TiO2(110), Phys. Rev. Lett., 87 (2001) 266104.
[24] M. Setvín, U. Aschauer, P. Scheiber, Y.-F. Li, W. Hou, M. Schmid, A. Selloni, U. Diebold, Reaction of O2 with Subsurface Oxygen Vacancies on TiO2 Anatase (101), Science, 341 (2013) 988-991.
[25] S. Peng, F. Gong, L. Li, D. Yu, D. Ji, T. Zhang, Z. Hu, Z. Zhang, S. Chou, Y. Du, S. Ramakrishna, Necklace-like Multishelled Hollow Spinel Oxides with Oxygen Vacancies for Efficient Water Electrolysis, J. Am. Chem. Soc., 140 (2018) 13644-13653.
[26] N. Son Truong, J.-M. Lee, Y. Yang, X. Wang, Excellent Durability of Substoichiometric Titanium Oxide As a Catalyst Support for Pd in Alkaline Direct Ethanol Fuel Cells, Ind. Eng. Chem. Res., 51 (2012) 9966-9972.
[27] S.J. Tauster, S.C. Fung, R.L. Garten, Strong metal-support interactions. Group 8 noble metals supported on titanium dioxide, J. Am. Chem. Soc., 100 (1978) 170-175.
[28] H. Tang, J. Wei, F. Liu, B. Qiao, X. Pan, L. Li, J. Liu, J. Wang, T. Zhang, Strong Metal–Support Interactions between Gold Nanoparticles and Nonoxides, J. Am. Chem. Soc., 138 (2016) 56-59.
[29] J.C. Matsubu, S. Zhang, L. DeRita, N.S. Marinkovic, J.G. Chen, G.W. Graham, X. Pan, P. Christopher, Adsorbate-mediated strong metal–support interactions in oxide-supported Rh catalysts, Nat. Chem., 9 (2017) 120-127.
[30] Y. Xie, K. Ding, Z. Liu, R. Tao, Z. Sun, H. Zhang, G. An, In Situ Controllable Loading of Ultrafine Noble Metal Particles on Titania, J. Am. Chem. Soc., 131 (2009) 6648-6649.
[31] G. Kresse, J. Hafner, Ab initio molecular dynamics for open-shell transition metals, Phys. Rev. B, 48 (1993) 13115-13118.
[32] G. Kresse, J. Furthmüller, Efficiency of ab-initio total energy calculations for metals and semiconductors using a plane-wave basis set, Comp. Mater. Sci., 6 (1996) 15-50.
[33] P.E. Blöchl, Projector augmented-wave method, Phys. Rev. B, 50 (1994) 17953-17979.
[34] G. Kresse, D. Joubert, From ultrasoft pseudopotentials to the projector augmented-wave method, Phys. Rev. B, 59 (1999) 1758-1775.
[35] J.P. Perdew, K. Burke, M. Ernzerhof, Generalized Gradient Approximation Made Simple, Phys. Rev. Lett., 77 (1996) 3865-3868.
[36] D. Wang, T. Sheng, J. Chen, H.-F. Wang, P. Hu, Identifying the key obstacle in photocatalytic oxygen evolution on rutile TiO2, Nat. Catal., 1 (2018) 291-299.
[37] A.A. Gokhale, S. Kandoi, J.P. Greeley, M. Mavrikakis, J.A. Dumesic, Molecular-level descriptions of surface chemistry in kinetic models using density functional theory, Chem. Eng. Sci., 59 (2004) 4679-4691.
[38] H. Aoki, D. Watanabe, N. Ooi, J.-H. Jeong, C. Kimura, T. Sugino, High Rate Etching of Ru and TaN using Electrochemical Reaction for Bevel Cleaning, ECS Trans., 16 (2009) 9-14.
[39] J. Mahmood, F. Li, S.-M. Jung, M.S. Okyay, I. Ahmad, S.-J. Kim, N. Park, H.Y. Jeong, J.-B. Baek, An efficient and pH-universal ruthenium-based catalyst for the hydrogen evolution reaction, Nat. Nanotech., 12 (2017) 441-446.
[40] J.J. Suñol, M.E. Bonneau, L. Roué, D. Guay, R. Schulz, XPS surface study of nanocrystalline Ti–Ru–Fe materials, Appl. Surf. Sci., 158 (2000) 252-262.
[41] F. Yang, S. Kundu, A.B. Vidal, J. Graciani, P.J. Ramírez, S.D. Senanayake, D. Stacchiola, J. Evans, P. Liu, J.F. Sanz, J.A. Rodriguez, Determining the Behavior of RuOx Nanoparticles in

Mixed-Metal Oxides: Structural and Catalytic Properties of RuO2/TiO2(110) Surfaces, Angew. Chem. Int. Ed., 50 (2011) 10198-10202.
[42] H. Madhavaram, H. Idriss, S. Wendt, Y.D. Kim, M. Knapp, H. Over, J. Assmann, E. Loffler, M. Muhler, Oxidation reactions over RuO2: A comparative study of the reactivity of the (110) single crystal and polycrystalline surfaces, J. Catal., 202 (2001) 296-307.
[43] J. Xu, W. Dong, C. Song, Y. Tang, W. Zhao, Z. Hong, F. Huang, Black rutile (Sn, Ti)O2 initializing electrochemically reversible Sn nanodots embedded in amorphous lithiated titania matrix for efficient lithium storage, J. Mater. Chem. A, 4 (2016) 15698-15704.
[44] C. Mao, F. Zuo, Y. Hou, X. Bu, P. Feng, In Situ Preparation of a Ti3+ Self-Doped TiO2 Film with Enhanced Activity as Photoanode by N2H4 Reduction, Angew. Chem. Int. Ed., 53 (2014) 10485-10489.
[45] G. Zhang, J. Zou, X. Xu, Reduced 3d Transition Metal Oxides Work as Solid-State Sources of Solvated Electrons and Directly Inject Electrons into Water for H2 Production under Mild Thermal or IR Excitation, Adv. Sustain. Syst., 2 (2018) 1700139.
[46] M. Fittipaldi, D. Gatteschi, P. Fornasiero, The power of EPR techniques in revealing active sites in heterogeneous photocatalysis: The case of anion doped TiO2, Catal. Today, 206 (2013) 2-11.
[47] C.P. Kumar, N.O. Gopal, T.C. Wang, M.-S. Wong, S.C. Ke, EPR Investigation of TiO2 Nanoparticles with Temperature-Dependent Properties, J. Phys. Chem. B, 110 (2006) 5223-5229.
[48] J. Xu, T. Liu, J. Li, B. Li, Y. Liu, B. Zhang, D. Xiong, I. Amorim, W. Li, L. Liu, Boosting the hydrogen evolution performance of ruthenium clusters through synergistic coupling with cobalt phosphide, Energy Environ. Sci., 11 (2018) 1819-1827.
[49] T. Shinagawa, A.T. Garcia-Esparza, K. Takanabe, Insight on Tafel slopes from a microkinetic analysis of aqueous electrocatalysis for energy conversion, Sci. Rep., 5 (2015) 13801.
[50] M. Ichise, Y. Nagayanagi, T. Kojima, J Electroanal Chem Interfacial Electrochem, 33 (1971) 253-265.
[51] C.L. Green, A. Kucernak, Determination of the Platinum and Ruthenium Surface Areas in Platinum−Ruthenium Alloy Electrocatalysts by Underpotential Deposition of Copper. I. Unsupported Catalysts, J. Phys. Chem. B, 106 (2002) 1036-1047.
[52] Y. Zheng, Y. Jiao, Y. Zhu, L.H. Li, Y. Han, Y. Chen, M. Jaroniec, S.-Z. Qiao, High Electrocatalytic Hydrogen Evolution Activity of an Anomalous Ruthenium Catalyst, J. Am. Chem. Soc., 138 (2016) 16174-16181.
[53] Z. Pu, I.S. Amiinu, Z. Kou, W. Li, S. Mu, RuP2-Based Catalysts with Platinum-like Activity and Higher Durability for the Hydrogen Evolution Reaction at All pH Values, Angew. Chem. Int. Ed., 56 (2017) 11559-11564.
[54] H. Zhang, P. An, W. Zhou, B.Y. Guan, P. Zhang, J. Dong, X.W. Lou, Dynamic traction of lattice-confined platinum atoms into mesoporous carbon matrix for hydrogen evolution reaction, Sci. Adv., 4 (2018).
[55] K. Nam, H. Chun, J. Hwang, K.-A. Min, B. Han, Pairing of Transition Metal Dichalcogenides and Doped Graphene for Catalytically Dual Active Interfaces for the Hydrogen Evolution Reaction, ACS Sustainable Chem. Eng., 8 (2020) 10852-10858.
[56] Y. Zheng, Y. Jiao, A. Vasileff, S.-Z. Qiao, The Hydrogen Evolution Reaction in Alkaline Solution: From Theory, Single Crystal Models, to Practical Electrocatalysts, Angew. Chem. Int. Ed., 57 (2018) 7568-7579.

[57] T. Funaioli, C. Cavazza, F. Marchetti, G. Fachinetti, Aqueous organometallic chemistry of ruthenium (II). Aquo carbonyl derivatives and related ethene hydrocarboxylation in fully aqueous solvent, Inorg. Chem., 38 (1999) 3361-3368.
[58] B. Liu, B.-L. Li, Y.-Z. Li, Y. Chen, S.-S. Bao, L.-M. Zheng, Lanthanide diruthenium (II, III) compounds showing layered and PtS-type open framework structures, Inorg. Chem., 46 (2007) 8524-8532.

Figure Captions

Fig. 1. (a) Schematic illustration of the synthesis of Ru/r-TiO_2 and Ru/TiO_2 catalysts. (b) XRD of Ru/r-TiO_2. (c) TEM image of Ru/r-TiO_2. The inset shows the size distribution of Ru nanoparticles. (d) Elemental mapping of Ru/r-TiO_2..

Fig. 2. (a) Ru 3d XPS of Ru/r-TiO_2, Ru/TiO_2, Ru/TiO_2-O, and Ru/r-TiO_2-HTO electrocatalysts. (b) Peak deconvolution of Ru 3d XPS of Ru/r-TiO_2, Ru/TiO_2, and metallic Ru black. (c) Ti 2p XPS of Ru/r-TiO_2 and Ru/TiO_2. (d) Electron paramagnetic resonance (EPR) spectra of Ru/r-TiO_2 and Ru/TiO_2..

Fig. 3. (a) HER polarization curves of Ru/r-TiO_2, Ru/TiO_2, Pt/C, Ru/C, Ti(III) oxide, TiO_2 and GC electrocatalysts in H_2-saturated 1.0 M KOH solution. (b) Overpotentials at 10, 20, and 100 mA cm^{-2} for Ru/r-TiO_2, Ru/TiO_2, Pt/C, and Ru/C electrocatalysts. (c) HER polarization curves of Ru/r-TiO_2, Ru/TiO_2, Ru/TiO_2-O and Ru/r-TiO_2-HTO electrocatalysts in H_2-saturated 1.0 M KOH solution. (d) Tafel plots obtained from the polarization curves in (a) and (c). (e) TOF values of Ru/r-TiO_2 and Ru/TiO_2. (f) Stability test of Ru/r-TiO_2 by 1000 potential cycles between -50 and 10 mV at 5 mV s^{-1}. The inset is stability test at a constant potential of 0.015 V for 10 h. Electrode rotating speed: 1600 rpm; H_2 flow rate: 80 sccm.

Fig. 4. (a) Charge density differences for Ru(0001)/TiO_2 (up) and Ru(0001)/r-TiO_2 (down) interfaces. The yellow region represents charge accumulation, and the light blue region indicates charge depletion at the isosurface value of 0.01 e $Bohr^{-3}$. (b) Free energy profiles for HER from aqueous water to H_2 on different surfaces. (c) Optimized structures of the intermediates and transition states at Ru(0001)/TiO_2 (up) and Ru(0001)/r-TiO_2 (down) interfaces. (d, e) The enlarged view of OH* adsorption on Ru(0001)/r-TiO_2 (d) and Ru(0001)/TiO_2 (e) interfaces. Green: Ru; grey: Ti; red: O; white: H.

Figures

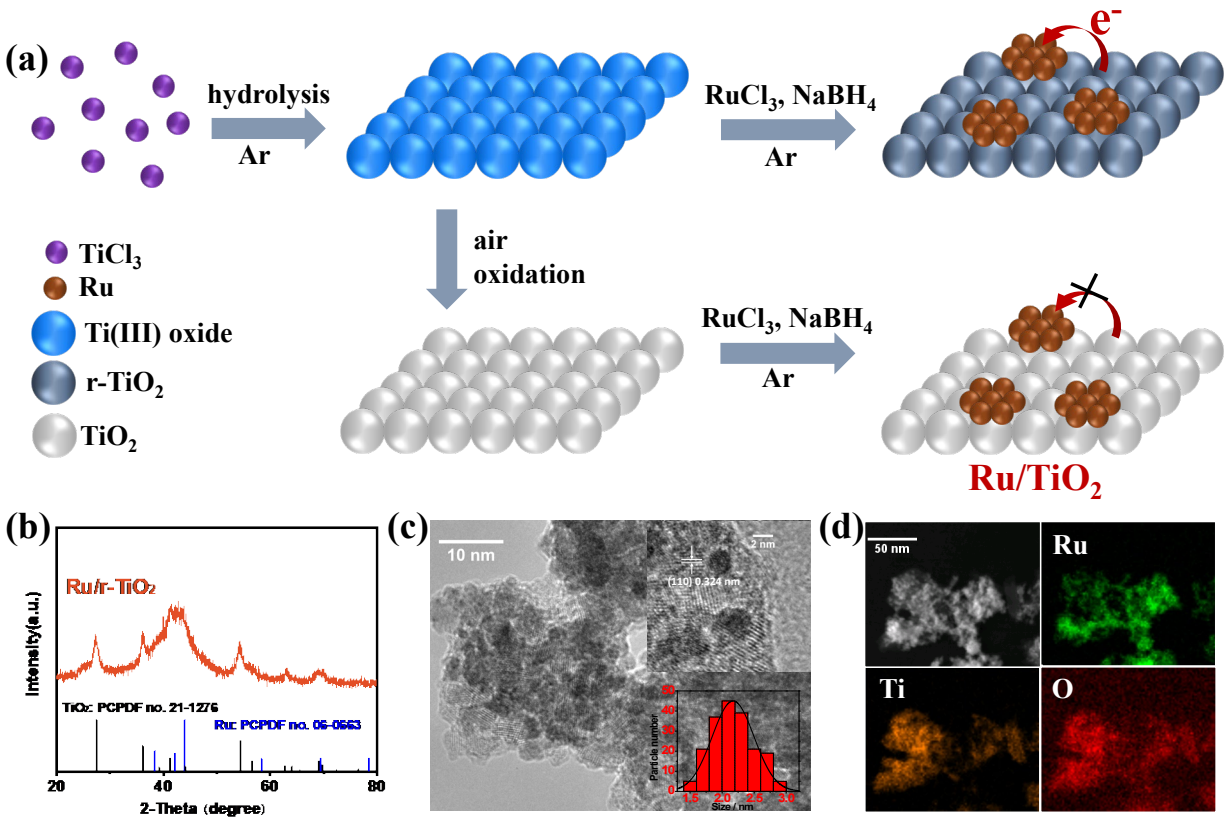

Fig. 1. (a) Schematic illustration of the synthesis of Ru/r-TiO_2 and Ru/TiO_2 catalysts. (b) XRD of Ru/r-TiO_2. (c) TEM image of Ru/r-TiO_2. The inset shows the size distribution of Ru nanoparticles. (d) Elemental mapping of Ru/r-TiO_2.

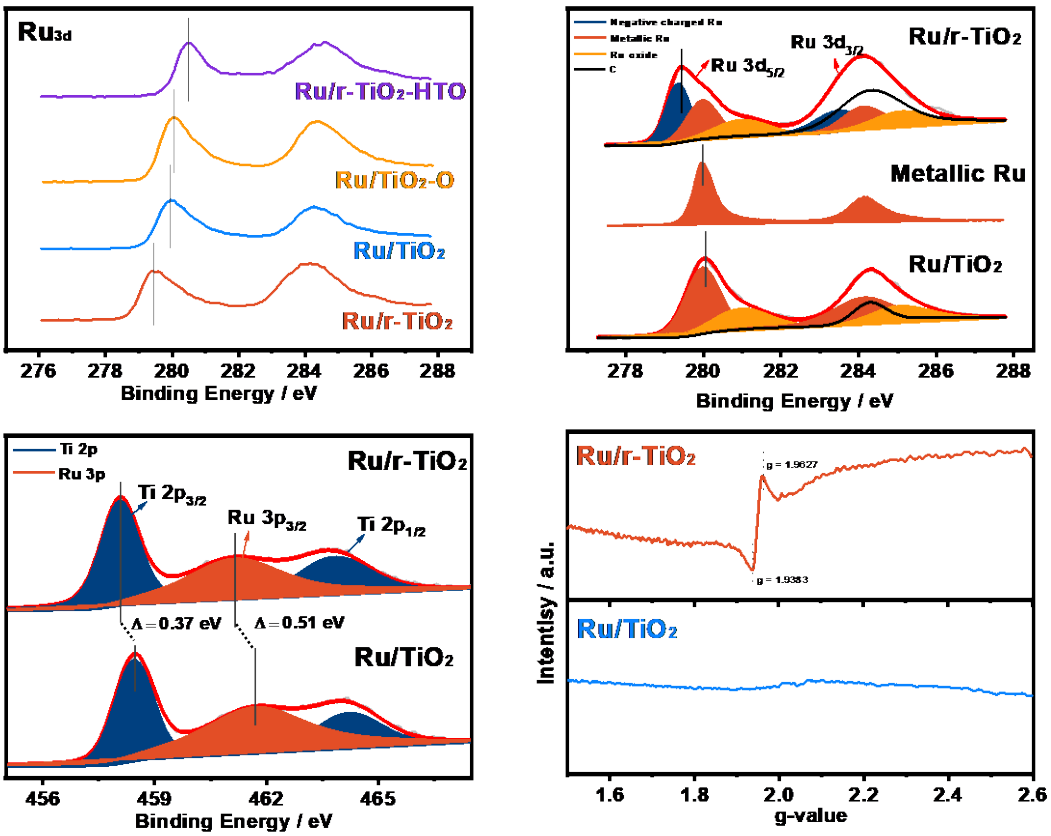

Fig. 2. (a) Ru 3d XPS of Ru/r-TiO_2, Ru/TiO_2, Ru/TiO_2-O, and Ru/r-TiO_2-HTO electrocatalysts. (b) Peak deconvolution of Ru 3d XPS of Ru/r-TiO_2, Ru/TiO_2, and metallic Ru black. (c) Ti 2p XPS of Ru/r-TiO_2 and Ru/TiO_2. (d) Electron paramagnetic resonance (EPR) spectra of Ru/r-TiO_2 and Ru/TiO_2.

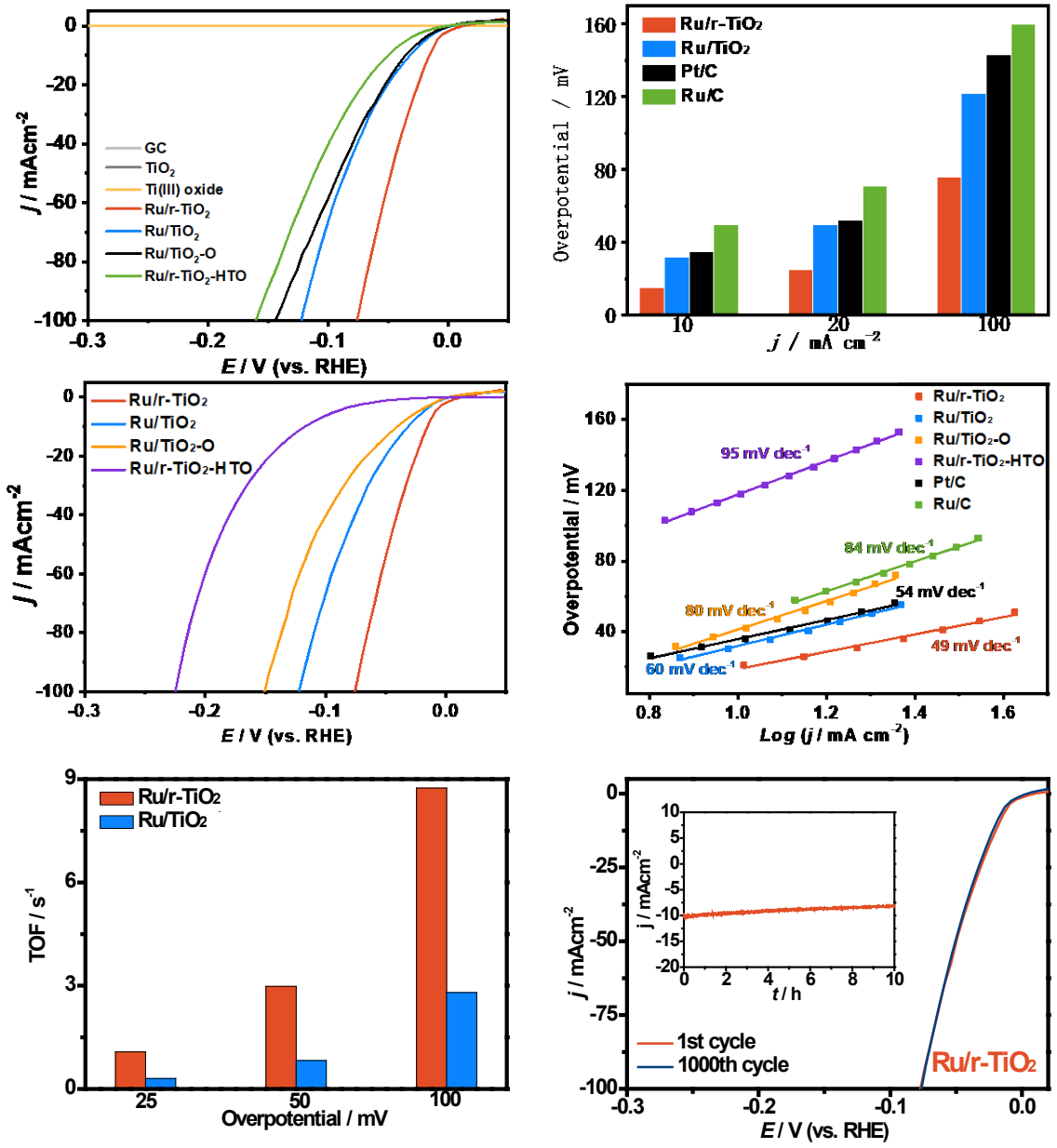

Fig. 3. (a) HER polarization curves of Ru/r-TiO_2, Ru/TiO_2, Pt/C, Ru/C, Ti(III) oxide, TiO_2 and GC electrocatalysts in H_2-saturated 1.0 M KOH solution. (b) Overpotentials at 10, 20, and 100 mA cm^{-2} for Ru/r-TiO_2, Ru/TiO_2, Pt/C, and Ru/C electrocatalysts. (c) HER polarization curves of Ru/r-TiO_2, Ru/TiO_2, Ru/TiO_2-O and Ru/r-TiO_2-HTO electrocatalysts in H_2-saturated 1.0 M KOH solution. (d) Tafel plots obtained from the polarization curves in (a) and (c). (e) TOF values of Ru/r-TiO_2 and Ru/TiO_2. (f) Stability test of Ru/r-TiO_2 by 1000 potential cycles between -50 and 10 mV at 5 mV s^{-1}. The inset is stability test at a constant potential of 0.015 V for 10 h. Electrode rotating speed: 1600 rpm; H_2 flow rate: 80 sccm.

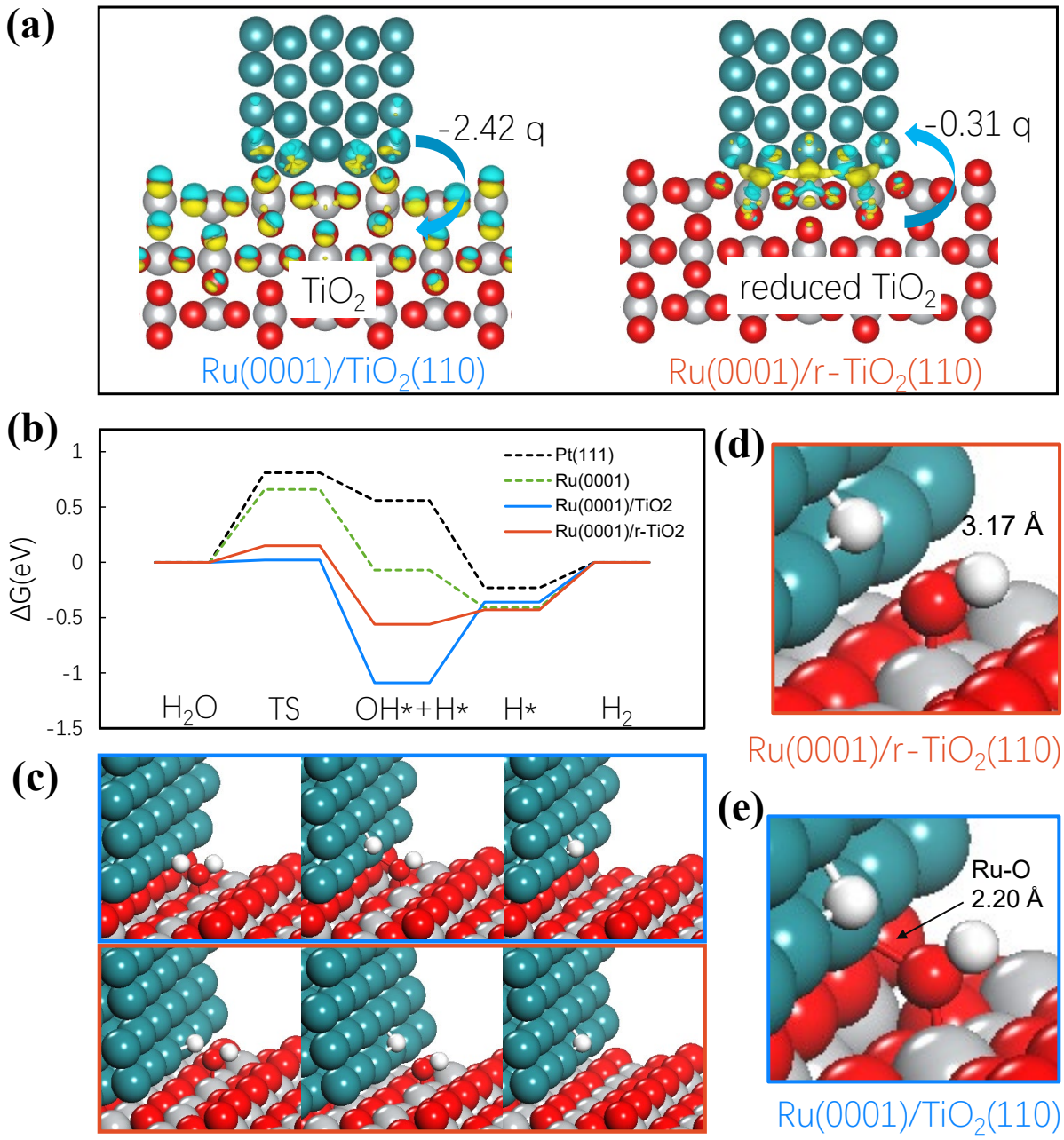

Fig. 4. (a) Charge density differences for Ru(0001)/TiO_2 (up) and Ru(0001)/r-TiO_2 (down) interfaces. The yellow region represents charge accumulation, and the light blue region indicates charge depletion at the isosurface value of 0.01 e $Bohr^{-3}$. (b) Free energy profiles for HER from aqueous water to H_2 on different surfaces. (c) Optimized structures of the intermediates and transition states at Ru(0001)/TiO_2 (up) and Ru(0001)/r-TiO_2 (down) interfaces. (d, e) The enlarged view of OH* adsorption on Ru(0001)/r-TiO_2 (d) and Ru(0001)/TiO_2 (e) interfaces. Green: Ru; grey: Ti; red: O; white: H.